In Situ Transmission Electron Microscopy Study of Bubble Behavior Near the Surface of Ice Crystals by Using a Liquid Cell with a Peltier-Cooling Holder

Running title: In situ TEM of ice crystals with Peltier cooling (48/50 characters)

Tomoya Yamazaki[1], Yuga Yashima[1], Hiroyasu Katsuno[1], Hiroya Miyazaki[2], Takashi Gondo[2], and Yuki Kimura[1,*]

[1]Institute of Low Temperature Science, Hokkaido University, Kita-19, Nishi-8, Kita-ku, Sapporo, 060-0819, Japan.

[2]Mel-Build Corporation, 2-11-36, Ishimaru, Nishi-ku, Fukuoka, 819-0025, Japan

*Corresponding author: E-mail: ykimura@lowtem.hokudai.ac.jp, TEL/FAX: +81-11-706-7666/+81-11-706-7666

Abstract:

Liquid-cell transmission electron microscopy (LC-TEM) is a unique technique that permits in situ observations of various phenomena in liquids with high spatial and temporal resolutions. One difficulty with this technique is the control of the environmental conditions at the observation area. Control of the temperature in the range from room temperature to minus several tens of degrees Celsius is desirable for controlling the supersaturation in various materials and for observing crystallization more easily. We have developed a cooling TEM specimen holder that uses Peltier devices and we have combined it with a liquid cell to realize accurate temperature control in LC-TEM. We evaluated this system by using water as a specimen. Motionless bubbles, shown to be voids containing pressurized gas, formed in the specimen some time after the temperature had reached −12 ℃. An electron-diffraction pattern showed that the specimen turned into ice Ih after the formation of these bubbles, confirming that our system works properly and can induce crystallization. In addition, we analyzed the behavior of bubbles formed in the ice Ih, and we discuss the formation of these bubbles and their internal pressure.

Key words: liquid-cell transmission electron microscopy, in situ observation, crystallization, radiolysis, ice, water, Peltier element, cooling holder

Introduction

Liquid-cell transmission electron microscopy (LC-TEM) is a technique that permits the observation of volatile samples, such as aqueous solutions, by transmission electron microscopy (TEM) (Ross, 2016). Because this technique can be used to observe various phenomena in solution at the nanoscale (de Jonge et al., 2019), it is promising for visualizing the events during the early stages of crystallization, such as the nucleation of crystals from solution. Recent studies using LC-TEM have revealed that the nucleation of crystals is a complex process in which various growth units, such as atoms or molecules, do not assemble one by one to form the nucleus of a crystal but, instead, form a crystal nucleus via intermediates such as amorphous or dense liquid (Nielsen et al., 2014; Patterson et al., 2015; Yamazaki et al., 2017; Ou et al., 2020). These facts clearly indicate that this method is promising for clarifying the previously inaccessible picture of nucleation.

However, it remains difficult to observe the moment of nucleation by LC-TEM. One reason for this is the scarcity of methods available for inducing crystallization within the observation area. To observe the crystallization, it is usually necessary to increase the supersaturation σ (defined as $\sigma = \ln(C/C_e)$, where C is the concentration and C_e is

49 the solubility) within the observation area to create the supersaturated conditions that
50 are necessary for crystallization to occur. To increase the supersaturation, it is clearly
51 necessary to increase the concentration of the solute and/or decrease its solubility. Such
52 an operation is difficult to perform within the observation area for LC-TEM. Increasing
53 the concentration of ions in LC-TEM has been achieved for some systems by using
54 radiolysis (Yuk et al., 2016; Yamazaki & Kimura, 2021). Radiolysis is the process by
55 which electrons impart part of their energy to a solution sample, especially a solvent,
56 resulting in the decomposition of the solvent to form active species that undergo
57 secondary chemical reactions with the surrounding solvent and solute molecules to
58 produce various chemical species that are not present in the initial solution (Schneider et
59 al., 2014; Ambrožič et al., 2019). This process permits the production of the chemical
60 species that are necessary for crystallization to occur, thereby generating supersaturated
61 conditions for the target crystals; however, the range of systems to which this technique
62 can be applied is very limited.

63 Another promising method for increasing the concentration within the observation
64 area involves the use of electrodes. A liquid cell with an amorphous silicon nitride
65 membrane can be equipped with electrodes to which an electrical signal can be applied.

66 One way in which these electrodes can be used in observing crystallization is to induce
67 an electrochemical reaction on them. This can, for example, permit the visualization of
68 electrodeposition on electrodes during a battery charge–discharge cycle (Mehdi et al.,
69 2015). Another way to use the electrodes is to create an electrical field around them that
70 induces electric-field-related phenomena such as dielectrophoresis (Pohl, 1951). It is
71 possible to induce dielectrophoresis in a liquid cell so that colloidal particles collect
72 around electrodes (Yamazaki et al., 2022). This is a promising method for increasing
73 particle concentrations in the region around the electrodes and could trigger
74 crystallization, although the development of this concept remains a work in progress.

75 In contrast to methods that increase concentration, methods that decrease solubility
76 generally involve changing the temperature of the observed system, and cooling is
77 particularly effective for most solution systems. Cooling experiments under TEM are
78 generally performed by using a refrigerant such as liquid nitrogen. TEM specimen
79 holders for this technique have heaters to maintain the temperature of the specimen by
80 controlling the balance of heat transfer between the heater and the refrigerant. With this
81 temperature-control system, it is difficult to maintain temperatures that are just below
82 room temperature because of an imbalance between the capacity of the heater and that

of the refrigerant. Such systems are useful in so-called cryo-TEM, where biological samples are frozen and supported in amorphous ice for observation (Dubochet et al., 1988). The range of applications of crystallization from a solution or a pure liquid (crystallization of a melt) through cooling with a liquid cell in TEM experiments is very limited (Tai et al., 2014).

For optical microscopy, cooling stages that use Peltier elements are commonly used in observing crystallization from solution (Dold et al., 2006). Temperature control by using Peltier devices is based on the Peltier effect, in which heat is absorbed or generated when an electric current is applied to a joint between different metals. In practice, when a direct current is applied to a Peltier device, one side of the device is cooled while the other side is heated. By controlling the amount of direct current, the temperature of the specimen and/or its stage can be controlled so that it remains at a desired temperature. This temperature-control system is accurate in principle, and the temperatures that can be controlled by such a system range from several tens to minus several tens of degrees Celsius, with an accuracy of ±0.1 °C. The key to successful cooling by using Peltier elements is the release of the heat that is produced by the elements. If insufficient heat is released from the heating side, it can be transferred to

100 the cooling side, resulting in inadequate cooling. Heat-dissipating fins and/or refrigerant
101 circulated by a pump can be used to remove the heat generated in the heated section of a
102 Peltier element.

103 We have developed a TEM cooling holder that uses a Peltier device and we have
104 established an experimental system that combines the holder with a liquid cell for
105 performing crystallization experiments on liquid specimen. To demonstrate the
106 effectiveness of our cooling system, we used water, which was expected to form ice
107 crystals upon cooling, as a liquid specimen, and we successfully observed the formation
108 of ice crystals. An initial broad examination also showed that bubbles that formed near
109 the surface of the ice displayed an interesting behavior, analysis of which provided clues
110 as to the conditions present within the ice and the liquid cell.

111

112 **Materials and Methods**

113 ***TEM and Electron-Beam Irradiation Conditions***

114 We used a transmission electron microscope (JEM-2100F; JEOL Ltd., Tokyo) with a
115 field-emission gun operated at an acceleration voltage of 200 kV. The TEM images and

videos were recorded by using a OneView IS TEM camera (Gatan, Inc., Pleasanton, CA). Energy-dispersive X-ray spectroscopy (EDS) for elemental analysis and mapping was performed using an EDS system (JEOL JED2300T) equipped with a silicon drift detector. The electron flux of the electron beam irradiating the specimen was controlled by using an electrostatic shutter (Electrostatic Dose Modulator; IDES, Inc., Pleasanton, CA) to produce a pulsed electron beam. The intensity of the pulsed electron beam followed a square-wave pattern with a frequency of 10^4 Hz. To reduce the overall intensity of a continuous electron beam of, for example, 1.0 e^- nm^{-2} s^{-1} to 0.1 e^- nm^{-2} s^{-1} (one tenth), during each 0.1 ms of the experiment, the electron beam is irradiated for 0.01 ms with no irradiation during the remaining 0.09 ms. The irradiation rate of the electron beam is expressed as a percentage along with the electron flux. In the previous example, the electron flux is denoted as 0.1 e^- nm^{-2} s^{-1} (10%). We measured the electron flux when the electrostatic shutter was used without any sample. From this value, we calculated the electron dose rate, and the values of the electron dose rate shown here are those of the electron beam before it penetrated the sample. The electron dose rate was calibrated by using a Faraday cage (JEOL Ltd., Tokyo, Japan). We used *DigitalMicrograph* (Gatan, Inc., Pleasanton, CA) and *imageJ* (Schneider et al., 2012) software to analyze the TEM images. We also used *Recipro* (Seto & Ohtsuka,

2022) to simulate electron-diffraction patterns.

The Peltier-Cooling TEM Holder

We have developed a Peltier-cooling TEM holder (Figs. 1a–c) that has a double stacked Peltier element inside the handle of the TEM holder (Fig. 1b), together with built-in heat-transfer rods that extend from the Peltier element to just before the sample stage, which can be replaced by other stages, depending on the required purpose (Fig. 1d–h). The holder is equipped with signal lines (Fig. 1b) to apply a dc electric current to the Peltier elements. A thermosensor and a heater are installed immediately before the sample stage inside the holder (not visible in Fig. 1). The thermosensor can measure the temperature near the sample location, including radiant head, and the temperature measured by the thermosensor was used to maintain the temperature at the desired value by balancing the outputs of the Peltier elements and a heater controlled by external signals. A refrigerant-type heat sink was used to dissipate the heat generated in the hot parts of the Peltier elements, and a low-pulsation chiller is used to circulate a refrigerant at −20 °C through the heat sink. For this purpose, the holder is also equipped with tubes

150 (Fig. 1c) for circulating the refrigerant. When this type of chiller is used, vibrations
151 caused by the circulation of the refrigerant are minimal. The actual temperature might
152 differ from that measured by the thermosensor: the difference will depend on the heat
153 capacity of the tip and other factors. We attempted to measure the temperature of the tip
154 in vacuum by using a platinum sensor directly attached to the tip. The temperatures
155 reported in this study are the values corrected by this measurement. As discussed below,
156 the temperature at which ice formed from water was consistent with that previously
157 reported, and the temperature measurement is therefore not significantly incorrect. Note,
158 however, because heat inflow from the platinum sensor was also possible, more-
159 accurate measurements of the temperature at the sample location would be desirable. It
160 is also desirable to calibrate the temperature by observing the phase transition of
161 materials that are less affected by the electron beam.

162

163 ***The Liquid Cell***

164 The liquid cell, installed at the tip of the holder, consisted of a copper liquid cell holder
165 with large and small O-rings (Fig. 1e), a 3-mm-diameter silicon chip (NT025A;

166 Norcada Inc., Edmonton, Canada) (Fig. 1f) and a 5-mm-square silicon chip (Fig. 1g)
167 (NX5025A; Norcada), with a 50 nm-thick amorphous silicon nitride (a-SiN_x)
168 membrane. Both windows measured 250 × 250 μm. The circular silicon chip was placed
169 on the small O-ring, and double-distilled water that had not been degassed was loaded
170 onto the chip as a specimen (Fig. 1f). The square silicon chip was then placed on the
171 circular silicon chip and the larger O-ring (Fig. 1g), and the copper lid was screwed on
172 (Fig. 1h). The water was thus encapsulated between the two a-SiN_x membranes. The a-
173 SiN_x membranes were placed so that they overlapped, allowing the electron beam to
174 penetrate through them to permit observation of the encapsulated water specimen.

175

176 **Results and Discussion**

177 ***Bubble Generation and Ice Formation***

178 We observed that ice crystallized in the liquid cell when the temperature was
179 reduced to −12 °C (Fig. 2). Initially, it was difficult to distinguish whether the water had
180 crystallized or not but, as described below, we were eventually able to identify
181 crystallization by means of the behavior of bubbles that formed in the sample. By

182 subsequently obtaining electron-diffraction patterns, we were able to identify the
183 formation of ice. Note that we use the term ‘bubble’ throughout to refer to a spherical
184 bright-contrast object observed in the ice crystal; this was actually a void, a type of
185 crystal defect, that contained gas, as will be discussed later.

186 The observation region of the liquid cell was filled with water, and no large air
187 bubbles were generated (Grogan et al., 2014) in the initial sample. The liquid cell was
188 gradually cooled to −12 °C and maintained at this temperature. About 3.5 minutes after
189 the temperature reached −12 °C, bright spots began to appear (Fig. 2b). The size of
190 these bright spots increased with time (Fig. 2c). The bright contrast of these spots
191 indicated that they were less dense than their surroundings. As we discuss later, we
192 concluded that these spots correspond to bubbles. In general, when such bubbles form in
193 an aqueous solution in a liquid cell they move or instantly grow so large that they cover
194 the entire field of view (Grogan et al., 2014). However, these bubbles grew slowly over
195 time and their centers did not move. We therefore concluded that the water had already
196 crystallized as ice.

197 When the temperature was raised toward 6 °C after the formation of these bubbles,
198 the ice crystal in the observation area shrank and the interface of the ice became

obscured; eventually, the observation area filled with water (Fig. 3 and Supplementary Video S1) because all the ice crystals in the liquid cell completely melted into water. When the ice reverted to water, the bubbles disappeared, suggesting that all the bubbles had dissolved in the water because water can dissolve gases, whereas bubbles are not readily incorporated into ice.

A selected-area electron-diffraction (SAED) pattern of the ice was acquired at −12 °C, as shown in Fig. 4. Note that it is generally difficult to obtain electron-diffraction patterns when this type of liquid cell is filled with a solvent, because the sample is too thick. We attempted to obtain a diffraction pattern when the liquid cell was filled with ice, but we could not obtain a clear diffraction pattern due to the thickness of the sample, which was probably of the order of several micrometers. We therefore searched for a large air bubble and we obtained a diffraction pattern through it (Fig. 4). The electron-diffraction pattern was consistent with that of ice Ih, as simulated by the *Recipro* software (Seto & Ohtsuka, 2022). We observed the presence of ice Ih at −12 °C, the same temperature as that found in a previous study in which ice Ih was observed at −12 °C by using a cooling TEM holder with a refrigerant and heater (Tai et al., 2014). Therefore, our temperature-control system combining a Peltier-cooling TEM holder and

a liquid cell worked successfully in the TEM observations.

Formation Routes of the Bubbles

There are two possible routes for the formation of gas bubbles during ice crystallization: either the gases are excluded from the water during ice crystallization in a degassing process or the gases are produced by radiolysis of the ice after crystallization.

After the ice had crystallized, we were often able to find an area where a large bubble had formed (Supplementary Fig. S1), through which the transmission of the electron beam was sufficient to permit the acquisition of an electron-diffraction pattern (Fig. 4). The EDS mapping images for oxygen and silicon show that neither element could be detected in such bubbles, whereas the surrounding was composed of oxygen, indicating ice (Supplementary Fig. S1). Assuming that the sample water was previously saturated with atmospheric gases, the ratio of the volume of the gas present to that of the water was calculated to be 50:1 (Supplementary Text S1). Because the window area accounted for less than 2% of the total liquid cell (the surface area of the small Si chip

was ~7 mm^2 whereas the area of the window was ~0.06 mm^2), if a large bubble that covered the entire window is formed, this can be explained by degassing of the water alone. When the ice reverted to water, these bubbles disappeared, suggesting that they had redissolved in the water (Fig. 3, Supplementary Video S1). The bubbles that formed only after the ice crystallization were primarily the result of degassing of the initial water sample as a result of ice crystallization.

As shown in Fig. 2, the bubbles continued to expand when the ice was irradiated with the electron beam. This suggests that radiolysis by the electron beam was the main source of gases after crystallization. When water/ice is irradiated with electrons, water molecules are excited and then undergo chemical reactions with surrounding water molecules. This process, known as radiolysis, results in the formation of various chemical species, including gas molecules such as hydrogen and oxygen (Schneider et al., 2014). The formation of bubbles by radiolysis is also supported by our observation that no bubbles formed in the ice regions not irradiated by the electron beam after crystallization. We therefore conclude that the bubbles formed in the ice crystal were the result of a radiolysis process. A schematic summarizing the two bubble-formation routes involving crystallization and electron-beam effects is shown in Supplementary Fig. S2.

In LC-TEM, radiolysis has significant effects on liquid specimens and on observing phenomena. Calculations of changes in the composition of liquid water resulting from radiolysis have shown that the production of hydrogen and oxygen depends on the electron dose rate (Schneider et al., 2014). Similarly, such gaseous products might be produced by the radiolysis of an ice specimen. The formation of bubbles in both ice and hydrated specimens has also been observed by cryo-TEM (Unwin & Muguruma, 1972; Dubochet et al., 1988). The formation and escape of bubbles (referred to as 'cavities' in the literature) under electron-beam irradiation have been observed in ice Ih at −80 °C (Unwin & Muguruma, 1972). Also, similar bubble formation has often been observed in hydrated organic specimens in ice under cryogenic conditions (Dubochet et al., 1988). The presence of hydrogen was confirmed by electron energy-loss spectroscopy (EELS) (Leapman & Sun, 1995). A similar analysis could provide insight into the composition of the bubbles produced in the present study and the chemical reaction pathway for the formation of these bubbles by radiolysis.

A Physical and Chemical View of the Formation of Bubbles in the Ice

265 Next, we will consider a physical view of the formation of bubbles in the crystals.
266 During radiolysis, lattice positions occupied by water molecules in an ice crystal
267 become vacant as a result of radiolytic decomposition, resulting in the formation of
268 vacancies. In the formation of a bubble, a plausible picture is that these vacancies
269 diffuse and aggregate to form a void that is filled by the gases generated by radiolysis.
270 The gases could diffuse through the crystal alone or together with the vacancies or
271 voids. Although a detailed model might provide a better account of the effects of gases
272 and defect sinks (Was, 2017), we assumed that the bubble-growth mechanism involves a
273 process of diffusion and aggregation of growth units (vacancies and/or vacancy and gas
274 molecule pairs); we were then able to predict the process that determines the growth
275 rate of the bubbles.

276 We measured the time dependence of the radius of one bubble (indicated by the
277 white arrow in Fig. 2) and we found that its radius increased almost linearly with time,
278 indicating that its growth rate R was constant (Fig. 5). The growth rate can be described
279 by the equation $R = K\sigma_{surf}$, where K is the kinetic coefficient and σ_{surf} is
280 supersaturation at the surface of the bubble (Chernov, 1984). The kinetic coefficient
281 represents the reaction process at the bubble's surface; this value will therefore be

282 constant if the environmental conditions, such as temperature, remain unchanged. The
283 supersaturation σ_{surf} can be expressed as $\sigma_{surf} = C_{surf} - C_{eq}$, where C_{surf} is the
284 concentration of growth units in ice at the surface of the bubble and C_{eq} is the
285 equilibrium concentration of growth units. The equilibrium concentration C_{eq} will also
286 be constant if the environmental conditions are unchanged. As the particles become
287 larger, the number of sites for the incorporation of growth units increases and the
288 concentration C_{surf} tends to decrease. In the present case, the constant growth rate
289 during the observation period suggests that bubble growth is rate-limited by the reaction
290 process at the surface of the bubble.

291 According to the literature (Schneider et al., 2014.), the electron flux in Fig. 2
292 corresponds to the dose rate of 10^5 Gy s^{-1} under our experimental conditions. At this
293 dose rate, the concentrations of hydrogen and oxygen at chemical equilibrium in the
294 irradiated area are approximately 10^{-5} and 10^{-6} M, respectively. If all the gas
295 components emerge as a bubble from a water volume of 1000 μm^3 (this assumes from a
296 volume of 10 × 10 × 10 μm^3, similar to our observation conditions) at this
297 concentration, the volume of the bubble would be ~0.2 μm^3 at atmospheric pressure and
298 −12 °C. Even if the gas is consumed for growing bubbles, the gas concentration is

maintained at this value on the millisecond scale because the solution is in chemical equilibrium. Therefore, the maximum gas production rate is estimated to be 200 μm^3 s^{-1}, which is sufficient to grow a bubble with a diameter of 1.8 μm (volume of ~24 μm^3) in 236 s. The value calculated under this assumption is consistent with the results of the present experiment. Note that this gas production rate is calculated for a thin film of water. Because the sample in our experiment is ice and thicker (multiple scattering of electrons should occur), the production rate should be different.

This might provide further insights into the details of the bubble-formation mechanism to measure the bubble growth rate as functions of the temperature and the dose rate.

Estimation of the State of the Ice and Its Environment by an Analysis of the Bubbles

In this section, we discuss details of the nature of the ice and its surrounding environment obtained by analyzing the bubbles. When all the liquid water had crystallized, the dissolved gases were excluded, and a gas–solid interface formed inside the liquid cell. Observations performed at −12 °C showed that the interface slowly

315 receded (Fig. 6 and Supplementary Video 2). While the interface was receding, bubble
316 growth was not clearly observed. In addition, the temperature increase in LC-TEM has
317 been estimated to be small (Grogan et al., 2014), and we did not observe any drastic
318 changes, such as boiling of water, induced by high temperatures. Therefore, this
319 recession might have been due to decomposition of the ice crystals through radiolysis,
320 with the radiolysis products, as well as forming bubbles, escaping from the interface
321 before being incorporated into bubbles.

322 The bubbles formed within the ice crystals remained stationary at constant
323 positions (the positions of the centers of the spheres did not change), and no movement
324 of the bubbles inside the crystals was clearly observed. Under these conditions, as the
325 surface of the ice crystal receded and the surface moved closer to the bubbles, the
326 bubbles were eventually ejected from the surface of the ice crystal. When bubbles began
327 to be ejected, they were observed to be moving and their shapes became deformed, so it
328 appeared that there might have been a liquid layer present on the surface. Here, we
329 discuss the state of the ice surface by analyzing the behavior of the bubbles.

330 First, let us assume the presence of a liquid layer on the surface of an ice crystal
331 about the size of a bubble (several hundreds of nanometers), from which the bubble

escapes. This is a similar situation to the case in which bubbles escape from the surface of bulk water at a flat gas–liquid interface. Note that a layer of liquid on the ice surface, commonly called the quasi-liquid layer, is not observed in this temperature region, and its thickness is less than 100 nm (Sazaki et al., 2022).

When a bubble with a size of a few tens of micrometers escapes from bulk water, the relaxation time of the water's surface has been experimentally determined to be several tens of microseconds (because the water surface generally oscillates during the relaxation, the time for one cycle of oscillation is taken as the relaxation time) (Lee et al., 2011). On the other hand, the relaxation time that we observed before the bubbles escaped from the surface and the surface was roughly flattened was about one second for bubbles with a diameter of 600 nm (Fig. 6). The measured relaxation time was therefore huge compared with that of bulk water. This discrepancy shows that ordinary water was not present on the surface of the ice. If a liquid layer is highly viscous, its relaxation time τ can generally be described by the expression $\tau = \mu h/\gamma$ (Bird et al., 2010), where μ is the viscosity, h is the distance between the interface and the surface of the air bubble, and γ is the surface tension. If we assume that the surface tension of water at −12 °C is 0.077 kg s^{-2} (Kalová & Mareš, 2018), a typical value of h is about

100 nm (Fig. 4), and the relaxation time is about 1 s, the viscosity of the liquid phase is 7.7×10^5 Pa s or 7.7×10^8 cP. This is highly viscous for a liquid, and its value is more than eight orders of magnitude higher than that of bulk water. Therefore, it is reasonable to infer that the surface remains in a solid state. It would be interesting to observe the ice surface at closely spaced temperatures around the melting point to identify the boundary between the liquid and solid phases.

If the surface is solid, the mass-transport process involved in restoring a flat surface can be estimated from the relaxation time of the surface. Immediately after bubble rupture, a hole is created in the surface of the ice, and the flat surface is eventually restored because the ice attempts minimize its surface energy. During this recovery process, the supply of molecules to the ice surface can be estimated by applying Herring's scaling law for sintering (Herring, 1950), which can be used to predict the process of mass transfer from the relationship between the relaxation time and the characteristic length power. We measured the dependence of the relaxation time on the bubble size (Fig. 7) and we found that it increased with the bubble size to the power 1.77. According to Herring's scaling law, this corresponds to a process of evaporation and condensation in which molecules that have evaporated into the gas

366 phase are taken up again at the surface (for which the power is approximately 2), and
367 not volume diffusion (for which the power is approximately 3). This result suggests that
368 the process of surface relaxation involves the release of water molecules from a
369 relatively unstable crystal and their reincorporation from the gas phase to form a surface
370 to minimize the surface energy.

371 If the ice surface is crystalline, its tensile strength can be used to estimate the
372 pressure inside the bubbles. In Fig. 4, a bubble with a radius of 200 nm ruptured when
373 the ice between the bubble and the environmental phase was 100 nm thick. Rupture
374 occurs when the stress generated by the internal pressure of a bubble exceeds the tensile
375 strength of the ice. In a thick-walled spherical container of thickness t, the maximum
376 stress due to the internal pressure caused by the enclosed gas is equal to the stress
377 applied at the inner wall of the container, and can be expressed by the following
378 equation:

379 $$\sigma_{inner} = p\frac{(r+t)^2 + r^2}{(r+t)^2 - r^2} \quad (1).$$

380 If we assume that the internal pressure inside the liquid cell is equal to atmospheric
381 pressure (0.1 MPa) and that the tensile strength of the ice is 1−2 MPa (Cuda & Ash,

1984), the pressure p ranges from 0.38 to 0.77 MPa, which is the same order of magnitude as atmospheric pressure. This is small compared with the pressure of ~10^3 atmospheres inside bubbles generated in water samples containing organic matter, as measured by EELS (Leapman & Sun, 1995). From a simple ratio, when two water molecules are converted into gases, two hydrogen molecules and one oxygen molecules are produced. The volume occupied by one water molecule in ice Ih is 0.32 nm^3, whereas the volume of one ideal gas molecule at one atmosphere is 41 nm^3. If three gas molecules are present in the space previously occupied by two water molecules, the local pressure would be about 200 atm. However, the diffusion coefficient of molecular hydrogen in ice Ih under similar condition to those of our study is 10^{-11} m^2 s^{-1} (Patterson & Saltzman, 2021), a value that is as large as that of macromolecules in aqueous solution. Therefore, interactions might occur between the bubble surface and hydrogen molecules that keep hydrogen within the bubble.

Application of the Cooling TEM Holders, and Perspectives

Our experimental system composed of the Peltier-cooling TEM holder and a liquid cell can be used to study phase transitions of liquids and crystallization from solutions (e.g., salt precipitation from solutions). In the current situation, we can use it to study the dynamics of the early stages of crystallization. Even in a thick solution layer where no bubbles are generated, we have measured the growth rate of crystals using a combination of a liquid cell and machine learning to detect crystallization (Katsuno et al., 2022). In this experiment, we captured a large change in growth rate in the early stages of crystallization. We speculate that this change in growth rate is due to a phase transition from a metastable phase to a stable phase. Our system is useful for studying the nucleation pathways to the most stable phase for various crystallization systems.

Thinning a sample liquid layer for high-resolution imaging is one of the future challenges for realizing the potential of our developed system. There are mainly two methods to produce a thin liquid layer in this type of liquid cell: generation of bubbles and the use of rectangular-slit window frames. The generation of bubbles in this type of liquid cell produces a thin layer of liquid (meniscus) on the membrane (Grogan et al., 2014). This procedure is necessary to attain high-

resolution images and electron diffraction patterns. Such a bubble is often generated without the experimenter realizing it. The presence of a thin liquid layer on the membrane is supported by indirect evidence such as the growth of crystals on the membrane. In addition, controlling the thickness of the bubble-induced liquid layer formed on the membrane is difficult. In practice, the liquid layer is sufficiently thin for high-resolution images to be acquired. With the second method (i.e., using rectangular-slit window frames), the thickness of the sample can be reduced somewhat by using rectangular-slit window frames and overlapping the window frame in a cross (Li et al., 2021). This type of liquid cell could be used in our system, and the spatial resolution would be improved at the corners where the windows overlap. However, controlling the thickness of the liquid in the entire liquid cell is difficult because of the bulging effect (Holtz et al., 2013). Controlling the liquid layer thickness over a large-scale area is a technical challenge not only for this system but also for liquid-cell TEM using a-SiN_x membranes.

Conclusion

We have developed a cooling TEM specimen holder that uses Peltier devices and we have combined it with a liquid cell to establish a temperature-controlled LC-TEM system. We crystallized water by using this system and we showed that the device operates correctly and can promote crystallization by decreasing the temperature. The growth of bubbles formed in ice Ih and their internal pressure have been discussed on the basis of the behavior of the bubbles. Bubbles in ice were formed by radiolysis, and their growth rate suggested that the kinetics of incorporation of growth units at the bubble–ice interface was the rate-limiting step for bubble growth. When the bubbles escaped from the ice surface, the surface appeared to consist of a liquid phase, but the relaxation time of the surface suggested that it remained as a solid. When Herring's scaling law was applied, the dependence of the relaxation time on the bubble sizes suggested that surface relaxation occurred by a process of evaporation and condensation. Based on the state of ice when the bubbles ruptured, the pressure inside the bubble was estimated to be in the range 0.38 to 0.76 MPa, assuming that the inside of the liquid cell was at atmospheric pressure.

In conclusion, our system can be used to investigate not only crystallization, but also physical properties and interfacial conditions based on dynamic behaviors through

448 in situ observations. The system will be useful in investigating crystallization from
449 aqueous solutions and, as shown in this study, it will help in achieving an understanding
450 of the properties of materials and phenomena that occur inside liquid cells to elucidate
451 the behavior of materials under observation. It should be possible to understand the
452 observed phenomena more deeply by examining the effect of the dose rate and the
453 temperature dependence.

454

455 **Acknowledgements**

456 We are grateful to Mr. S. Ikezawa (Mel-Build Corporation) for his support in facilitating
457 the smooth progress of the research. This work was supported by JSPS KAKENHI,
458 grants numbers JP20H02580 and JP20H05657.

459

460 **References**

461 Ambrožič, B., Prašnikar, A., Hodnik, N., Kostevšek, N., Likozar, B., Rožman, K. Ž. &
462 Šturm, S. (2019). Controlling the radical-induced redox chemistry inside a liquid-cell
463 TEM. Chem Sci 10, 8735–8743.

464 Bird, J. C., de Ruiter, R., Courbin, L. & Stone, H. A. (2010). Daughter bubble cascades
465 produced by folding of ruptured thin films. Nature 465, 759–762.

466 Chernov, A. A. (1984). Modern Crystallography III: Crystal Growth. Berlin: Springer Verlag.

467 Cuda, V. Jr. & Ash, R. L. (1984). Development of a uniaxial ice tensile specimen for low
468 temperature testing. Cold Reg Sci Technol 9, 47–52.

469 Dold, P., Ono, E., Tsukamoto, K. & Sazaki, G. (2006). Step velocity in tetragonal lysozyme
470 growth as a function of impurity concentration and mass transport conditions. J Cryst
471 Growth 293, 102–109.

472 Dubochet, J., Adrian, M., Chang, J.-J., Homo, J.-C., Lepault, J., McDowall, A. W. & Schultz,
473 P. (1988). Cryo-electron microscopy of vitrified specimens. Q Rev Biophys 21, 129–
474 228.

475 Grogan, J. M., Schneider, N. M., Ross, F. M. & Bau, H. H. (2014). Bubble and pattern
476 formation in liquid induced by an electron beam. Nano Lett 14, 359–364.

477 Herring, C. (1950). Effect of change of scale on sintering phenomena. J Appl Phys 21, 301–
478 303.

479 Holtz, M. E., Yu, Y., Gao, J., Abruña, H. D. & Muller, D. A. (2013). In situ electron energy-
480 loss spectroscopy in liquids. Microsc Microanal 19, 1027–1035.

481 de Jonge, N., Houben, L., Dunin-Borkowski, R. E. & Ross, F. M. (2019). Resolution and
482 aberration correction in liquid cell transmission electron microscopy. Nat Rev Mater 4,
483 61–78.

484 Kalová, J. & Mareš, R. (2018). The temperature dependence of the surface tension of water.
485 AIP Conf Proc 2047, 020007.

486 Katsuno, H., Kimura, Y., Yamazaki, T. & Takigawa, I. (2022). Early detection of nucleation
487 events from solution in LC-TEM by machine learning. Front. Chem. 10, 818230.

488 Leapman, R. D. & Sun, S. (1995). Cryo-electron energy loss spectroscopy: Observations on
489 vitrified hydrated specimens and radiation damage. Ultramicroscopy 59, 71–79.

Lee, J. S., Weon, B. M., Park, S. J., Je, J. H., Fezzaa, K. & Lee, W. K. (2011). Size limits the formation of liquid jets during bubble bursting. Nat Commun 2, 367.

Li, X., Mitsuishi, K. & Takeguchi, M. (2021). Fabrication of a liquid cell for in situ transmissions electron microscopy. Microscopy (Oxford, U. K.) 70, 327–332.

Mehdi, B. L., Qian, J., Nasybulin, E., Park, C., Welch, D. A., Faller, R., Mehta, H., Henderson, W. A., Xu, W., Wang, C. M., Evans, J. E., Liu, J., Zhang, J. G., Mueller, K. T. & Browning, N. D. (2015). Observation and quantification of nanoscale processes in lithium batteries by operando electrochemical (S)TEM. Nano Lett 15, 2168–2173.

Nielsen, M. H., Aloni, S. & de Yoreo, J. J. (2014). In situ TEM imaging of $CaCO_3$ nucleation reveals coexistence of direct and indirect pathways. Science 345, 1158–1162.

Ou, Z., Wang, Z., Luo, B., Luijten, E. & Chen, Q. (2020). Kinetic pathways of crystallization at the nanoscale. Nat Mater 19, 450–455.

Patterson, J. D. & Saltzman, E. S. (2021). Diffusivity and solubility of H_2 in ice Ih: Implications for the behavior of H_2 in polar ice. J Geophys Res: Atmos 126, 1–14.

Patterson, J. P., Abellan, P., Denny, M. S. Jr., Park, C., Browning, N. D., Cohen, S. M.,

505 Evans, J. E. & Gianneschi, N. C. (2015). Observing the growth of metal-organic
506 frameworks by in situ liquid cell transmission electron microscopy. J Am Chem Soc
507 137, 7322–7328.

508 Pohl, H. A. (1951). The motion and precipitation of suspensoids in divergent electric fields. J
509 Appl Phys 22, 869–871.

510 Ross, F. M. (Ed.) (2016). Liquid Cell Electron Microscopy. New York: Cambridge
511 University Press.

512 Sazaki, G., Murata, K., Asakawa, H., Nagashima, K., Nakatsubo, S. & Furukawa, Y. (2022).
513 The emergence of drop-type and thin-layer-type quasi-liquid layers on ice crystal
514 surfaces and their thermodynamic origin. J Cryst Growth 597, 126853.

515 Schneider, C. A., Rasband, W. S. & Eliceiri, K. W. (2012). NIH Image to ImageJ: 25 years of
516 image analysis. Nat Methods 9, 671–675.

517 Schneider, N. M., Norton, M. M., Mendel, B. J., Grogan, J. M., Ross, F. M. & Bau, H. H.
518 (2014). Electron–water interactions and implications for liquid cell electron microscopy.
519 J Phys Chem C 118, 22373–22382.

520 Seto, Y. & Ohtsuka, M. (2022). ReciPro: Free and open-source multipurpose crystallographic
521 software integrating a crystal model database and viewer, diffraction and microscopy
522 simulators, and diffraction data analysis tools. J Appl Crystallogr 55, 397–410.

523 Tai, K., Liu, Y. & Dillon, S. J. (2014). In situ cryogenic transmission electron microscopy for
524 characterizing the evolution of solidifying water ice in colloidal systems. Microsc
525 Microanal 20, 330–337.

526 Unwin, P. N. T. & Muguruma, J. (1972). Electron microscope observations on the defect
527 structure of ice. Phys Status Solidi A 14, 207–216.

528 Was, G. S. (2017). Fundamentals of Radiation Materials Science: Metals and Alloys. Berlin:
529 Springer.

530 Yamazaki, T. & Kimura, Y. (2021). Radiolysis-induced crystallization of sodium chloride in
531 acetone by electron beam irradiation. Microsc Microanal 27, 459–465.

532 Yamazaki, T., Kimura, Y., Vekilov, P. G., Furukawa, E., Shirai, M., Matsumoto, H., Van
533 Driessche, A. E. S. & Tsukamoto, K. (2017). Two types of amorphous protein particles
534 facilitate crystal nucleation. Proc Natl Acad Sci U S A 114, 2154–2159.

Yamazaki, T., Niinomi, H. & Kimura, Y. (2022). Feasibility of control of particle assembly by dielectrophoresis in liquid-cell transmission electron microscopy. Microscopy (Oxford, U. K.) 71, 231–237.

Yuk, J. M., Zhou, Q., Chang, J., Ercius, P., Alivisatos, A. P. & Zettl, A. (2016). Real-time observation of water-soluble mineral precipitation in aqueous solution by in situ high-resolution electron microscopy. ACS Nano 10, 88–92.

Figure legends

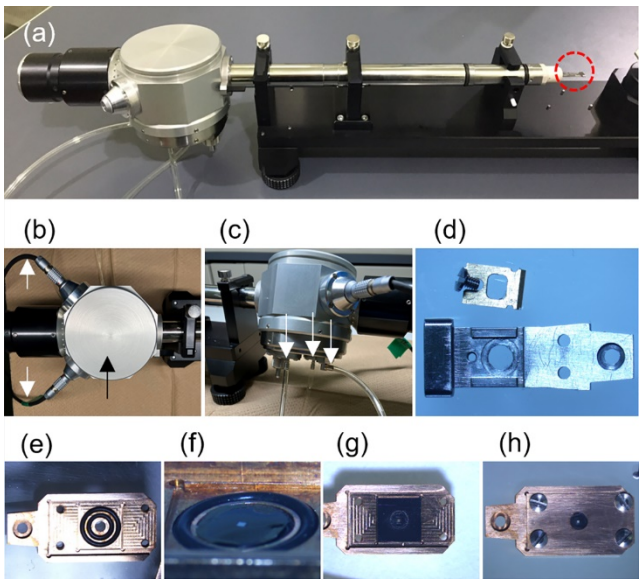

Figure 1. The Peltier holder and the procedure for assembly of the liquid cell. The liquid cell is assembled at the tip of the developed Peltier-cooling TEM holder, circled by the red dashed line (a). The Peltier device was installed inside the handle of the holder, as indicated the black arrow in (b), and the current is supplied and the temperature measurements are performed by using the signal lines indicated by the white arrows in (b). For circulation of the refrigerant, there are three ports indicated by white arrows in (c), two for circulation and one for removal of air bubbles by a syringe (c). The sample stage at the tip of the holder can be changed for samples on a conventional 3 mmΦ grid (d) or for liquid-cell experiments (e–h). The liquid-cell holder is made of copper on which the large and small O-rings are placed (e). A square Si chip

556 is placed on top of the small Si chip (f) and the large O-ring (g). The copper lid is then

557 positioned and tightened in place by screws (h).

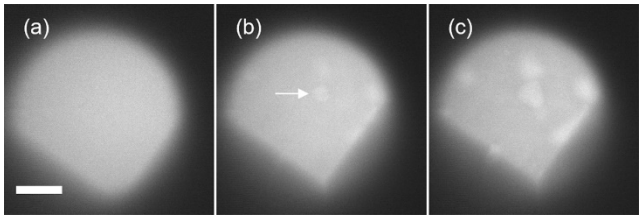

558

559 **Figure 2.** A series of bright-field TEM images showing the formation of bubbles in ice.

560 The outer circular dark area is the shadow of the condenser aperture. Nothing is visible

561 in the water sample at −8 °C (a). The sample was continuously observed at an electron

562 flux of 1.8 e^{-} nm^{-2} s^{-1} (11%). The temperature was lowered from −8 °C to −12 °C over

563 3.5 minutes, and after another 3.5 minutes at –12 °C, the formation of a bubble

564 (indicated by the white arrow) was clearly observed (b). The bubble grew larger for the

565 next 1.5 minutes (c). The scale bar is 5 μm, and all images are on the same scale.

566

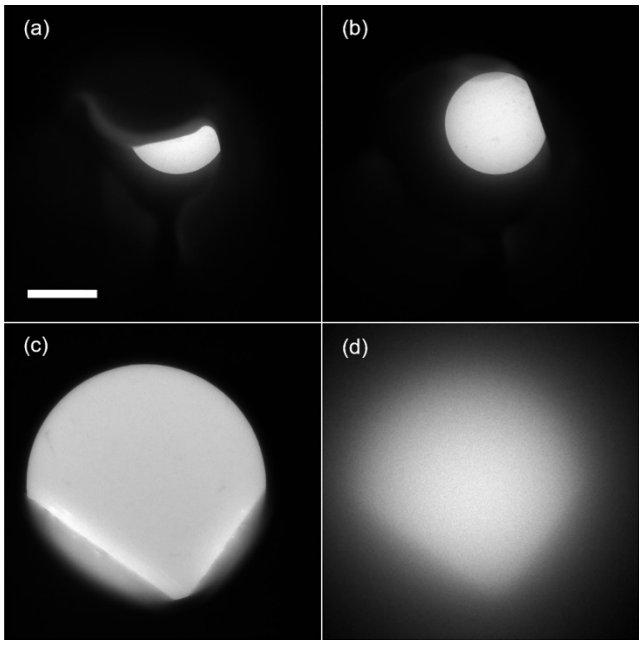

Figure 3. Dissolution of ice when the temperature was increasing toward 6 °C. These bright-field TEM images are from frames of Supplementary Video S1. At 0 s, with a selected-area diffraction aperture, ice was observed as a dark object (a). The ice receded and disappeared from the field of view at 2.7 s (b). After removing the selected-area aperture, no ice was present in the entire field of view at 5.2 s (c), and the field of view was filled with water at 7.2 s (d). The circular object in (c) is the condenser aperture. The electron flux was 17 e^{-} nm^{-2} s^{-1} (100%). The scale bar is 5 μm and all images are on the same scale.

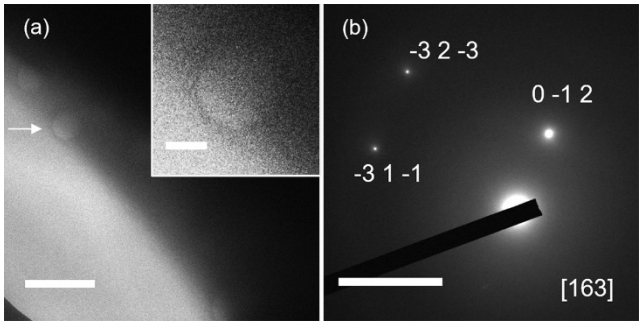

Figure 4. Identification of a formed crystal. The SAED pattern was acquired from the region of the crystal with the air bubble indicated by the white arrow in (a). The bright area in the lower left is the region where the large bubble was formed, and the dark area in the upper left corresponds to the ice crystal for which the SAED pattern was recorded. The inset is an enlarged image of the bubble. This bubble was just about to rupture, and these images were acquired at the point where the ice's crystal surface was nearly parallel to the electron beam. The diameter of the bubble was about 400 nm, and the thinnest part of the ice separating the bubble from the gas phase was about 100 nm. The SAED pattern corresponds to the [163] SAED pattern of ice Ih (b). The electron flux was 65 e^{-} nm^{-2} s^{-1} (50%). The scale bars are 1 μm (a) 200 nm (a, inset), and 5 nm^{-1} (b).

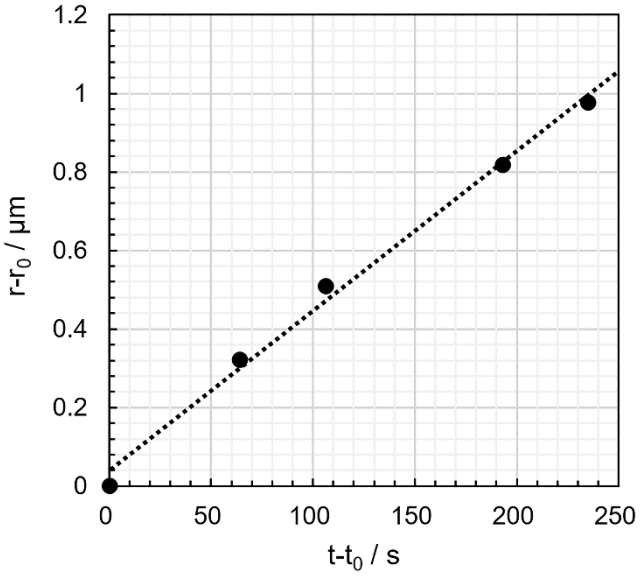

590

591 **Figure 5.** Change in the bubble size with time at an electron flux of 1.8 e^{-} nm^{-2} s^{-1}

592 (11%) at −12 °C. Because the time of the bubble occurrence was unknown, the plots

593 were produced by subtracting the size and time for the first bubble.

594

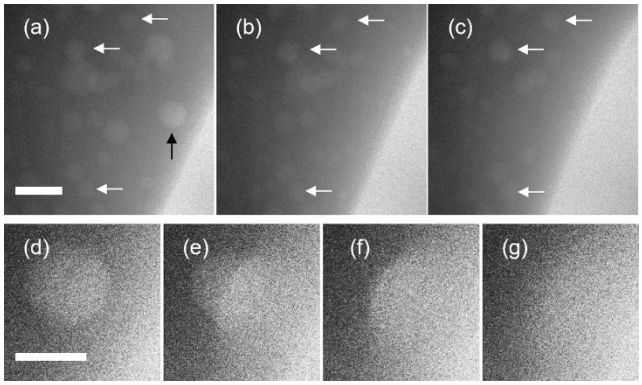

595

596 **Figure 6.** Recession of the ice surface and subsequent escape of bubbles. These bright-

597 field TEM images are frames from Supplementary Video S2. Many bubbles were

formed in the ice at 0 s (a). The ice surface in the gas phase appears as the straight line in the lower right of (a), and this receded after 15 s (b) and 30 s (c), even though the bubbles were not moving (indicated by the white arrows). A magnified image of the bubble indicated by the black arrow in (a) is shown in (d), and the subsequent escape process of the bubble is shown in (e–g). The rupture of the bubble began immediately after 0 s (d), progressed through 0.4 s (e) and 0.8 s (f), and was almost complete after 1.2 s (g). The electron flux was 89 e^{-} nm^{-2} s^{-1} (100%). The scale bar is 1 μm (a) and (a–c) are on the same scale. The scale bar is 500 nm (d) and (d–g) are on the same scale.

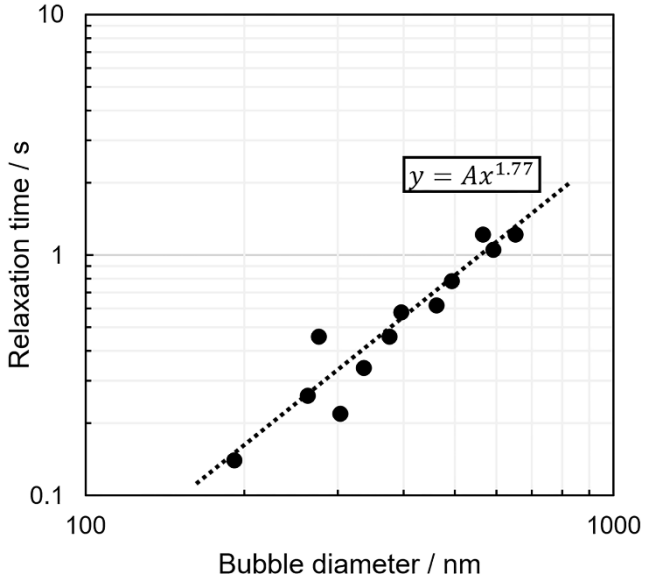

Figure 7. Dependence of the bubble size on the relaxation time for bubble rupture. The measurements were made on the bubbles shown in Supplementary Video S2. The power function $y = Ax^B$ was fitted with $A = 1.3 \times 10^{-5}$ and $B = 1.77$.